Research Article Vol. 32, No. 3 / 29 Jan 2024 / Optics Express 3278
Optics EXPRESS

1.3-μm identical active electro-absorption modulated laser with quantum well intermixed passive waveguide

SEUNGCHUL LEE,* NAMJE KIM, MIRAN PARK, AND O-KYUN KWON

Photonic/Wireless Devices Research Division, Electronics and Telecommunications Research Institute, 218 Gajeong-ro, Yuseong-gu, Daejeon, Republic of Korea
sclee@etri.re.kr

Abstract: Quantum well intermixing (QWI) is an effective method for simple and well-defined monolithic integration of photonic devices. We introduce an identical-active electro-absorption modulated laser (IA-EML) with optimized QWI, which is applied to reduce the absorptive waveguide region. To determine the optimal intermixed IA-EML structure, we conduct a comparative analysis between the cases of an IA-EML with only an intermixed waveguide region and with both intermixed waveguide and electro-absorption modulator (EAM) regions, as well as the case without QWI. The results reveal that the intermixed region effectively inhibits the absorption in the waveguide. In particular, the IA-EML with only waveguide intermixing exhibits superior modulation characteristics with low driving voltages and a high extinction ratio. Our work provides an attractive approach for suppressing the absorptive waveguide region in the IA-EML to enhance modulation performance and to develop photonic integrated circuits with a simplified process.

1. Introduction

Fifth and sixth-generation access networks rely on optical communication network technologies. These networks provide high capacity, high data rates, and low latency through the use of photonic devices such as laser diodes (LDs), modulators, amplifiers, and waveguides (WGs) [1–4]. In particular, LDs are the most crucial components of the networks, and various types of directly modulated lasers (DMLs) and electro-absorption modulated lasers (EMLs) are being actively researched [4–6]. In the case of DMLs, they do not require a separate modulator, as modulation occurs by directly injecting alternating current into the laser. For this reason, DMLs have frequency chirping characteristics and a relatively narrow bandwidth compared to EMLs [7,8]. On the other hand, EMLs include an electro-absorption modulator (EAM), reducing frequency chirping and increasing bandwidth, making them suitable for settled high-speed modulation. Thus, EMLs are preferred for high-speed optical communication systems.

For EML fabrication, one of the most preferred active layers is an InAlGaAs-based multi-quantum well (MQW). InAlGaAs has been widely used as the MQW materials due to its larger conduction band offset and smaller valence band offset compared to InGaAsP [9,10]. These advantages result in superior saturation characteristics and a better extinction ratio (ER) for EAM as well as high-temperature operation capabilities of EML [10–12]. However, InAlGaAs MQW is unsuitable for a conventional butt-joint regrowth process, which entails deep etching and regrowth of each MQW layer, such as LD, EAM, and WG. This is because Al oxidation not only occurs easily but also leads to reduced device reliability and deteriorated laser performance [13–15]. Moreover, etching and regrowth conditions should be controlled intricately and precisely to achieve high-quality butt-joint interfaces between several integrated components with minimal scattering loss. Such drawbacks directly impact the yield and cost of the device in a detrimental

#501764 https://doi.org/10.1364/OE.501764
Journal © 2024 Received 1 Aug 2023; revised 7 Dec 2023; accepted 8 Jan 2024; published 17 Jan 2024

Optics EXPRESS

manner. To overcome the limitation caused by butt-joint regrowth steps of InAlGaAs MQW, the identical active EML (IA-EML) has been proposed, which utilizes the same active layer for the entire EML structure, eliminating the need for numerous butt-joint regrowth processes [16–20]. However, the IA-EML suffers from unwanted absorption in the WG region between the LD and EAM, leading to degraded modulation characteristics of the EAM. Ultimately, it is the well-known consequence that removing the absorptive WG is essential to achieve high-speed modulation and a wide operation range of LD and EAM [21,22]. A significant difference between the absorption wavelength of the MQW and the lasing wavelength of the LD can prevent absorption in the WG. However, this approach may increase the driving voltage of the EAM, which can restrict the operating range for a sufficient ER. Additionally, the large difference between the gain spectrum and the lasing wavelength of the LD makes it challenging to obtain the necessary gain for lasing. These constraints can further impede the performance of EMLs and the flexibility of integrating additional components, such as amplifiers, in the IA-EML. Therefore, eliminating WG absorption in the IA-EML is indispensable for attaining adequate gain, ER, and high-speed modulation with the proper EAM driving voltage range.

Selective area growth (SAG) and quantum well intermixing (QWI) are two representative methods for adjusting the wavelength of the MQW without a regrowth process [23–27]. These techniques have been widely applied in the fabrication of photonic integrated circuit (PIC) devices [28–31]. SAG induces the decrease of the bandgap by varying the growth rate and chemical composition according to the dielectric thin film pattern in the first growth step of the MQW [32,33]. This method allows for the fabrication of an EML by placing the wavelength of the LD region at a longer wavelength than that of the WG and EAM. In contrast, QWI increases the bandgap of active layers, which is directly conducted for the adjustment of WG and EAM regions [34]. Ultimately, by appropriately utilizing SAG and QWI techniques, the monolithic integration of numerous active and passive components can be simply fabricated by regrowth-free processes [35–37].

Particularly, QWI can create distinct blue-shifted regions with discontinuous boundaries and no height differences. These blue-shifted regions reduce the absorption in the WG by producing passive regions and also aid in enhancing the characteristics of the EAM [38,39]. Therefore, it is possible to design an optimized WG and EAM structure without the intervention of the LD. In addition, the flat surface facilitates the convenient fabrication of grating structures and subsequent epitaxial growth. One of the QWI methods, impurity-free vacancy enhanced disordering (IFVD), involves injecting vacancies of the dielectric thin film into the MQW to induce a compositional change at the MQW interface [26,27,36]. Prior to the implementation of intermixing, to prevent damage to the growth layers, such as the MQW and separate confinement heterostructure (SCH), the entire surface of the wafer is covered with an InGaAs sacrificial layer, and a SiO_2 layer is deposited in specific areas by plasma-enhanced chemical vapor deposition (PECVD) to inhibit QWI of InAlGaAs MQW. Therefore, QWI is capable of controlling the energy bandgap of a particular region with a well-defined boundary. In the IFVD process, the deposition of sputtered SiO_2 generates vacancy defects that subsequently diffuse into the MQW during rapid thermal annealing (RTA). This results in changes in the material composition of the MQW by intermixing well and barrier atoms. Unlike other ion implantation intermixing methods, IFVD does not cause electrical and optical loss of the device, as it induces interstitial disordering without the intervention of impurities. By incorporating QWI into IA-EML fabrication, it is possible to simply adjust without butt-joint regrowth and an uneven surface, while maintaining high coupling efficiency and low transmission loss between individual unit devices.

In this study, we propose a method to eliminate WG absorption in the IA-EML by applying QWI. Additionally, we compared IA-EMLs with and without QWI in the EAM region to confirm the optimized configuration for modulation characteristics. First, we modified the QWI process to avoid any adverse effects on the MQWs and device performance beyond adjusting the bandgap by

Optics EXPRESS

precise intermixing. We then analyzed the optical characteristics of both as-grown and intermixed MQWs and verified the static and dynamic characteristics at 25 and 45°C. The intermixed MQW has a photoluminescence (PL) spectrum that is blue-shifted by approximately 20 nm compared to the as-grown MQW. By examining non-return-to-zero (NRZ) and pulse amplitude modulation 4-level (PAM4) eye diagrams and EO response, we confirmed that the IA-EML operates without the influence of WG absorption even when detuning between the gain and lasing wavelength is less than 25 nm. Furthermore, we observed that the driving voltage, extinction ratio (ER), 3 dB bandwidth, and transmitter and dispersion eye closure quaternary (TDECQ) are optimized at 45°C as well as 25°C when only the WG is intermixed. Our research offers a simple method to eliminate the absorptive WG in the IA-EML, which could be essential for the development of an ultra-high-speed EML and various PIC devices.

2. QWI for IA-EML device application

Before fabricating the IA-EML, we conducted the QWI process on an identical MQW. The QWI induced by the IFVD method was implemented before the growth of the p-cladding layer. Most conventional QWI processes involve sputtering after p-clad growth, with a thickness exceeding 1 μm. As a result, high energy is required during sputtering and RTA to induce intermixing at the active layer, and this can lead to a collapse of the crystal quality and problems such as residual defects and damage to the epitaxial layer. We modified the QWI process to execute it as close as possible to the MQW, ensuring minimal energy, with the aim of eliminating potential defects and damage in the active layer. Furthermore, it minimizes the impact of rapidly diffusing species, such as Zn dopant in the p-cladding layer [40].

First, we grew an InGaAs sacrificial layer on an InP cap after fabricating the grating structure. The distance between the MQW and the sacrificial layer was less than 300 nm. Subsequently, mask patterns were formed using PECVD SiO_2 to define the regions for inhibiting QWI. Next, we deposited a 50 nm thick layer of sputtered SiO_2 and conducted RTA at 700 °C for 120 seconds. Upon completing QWI, all InGaAs and SiO_2 thin films were wet-etched to implement the growth of p-cladding and ohmic contact layers.

We sought to verify the application of QWI not only in the WG region but also in the EAM. Therefore, we aimed to avoid an excessive blue-shift and determined QWI conditions with minimal damage to the active layer, resulting in an approximately -20 nm peak shift. Figure 1(a) indicates the PL peak shift after the QWI process, depending on the thickness of the PECVD SiO_2 protection layer. We compared conditions between the bare InGaAs sacrificial layer and samples with SiO_2 layers having thicknesses of 500 and 1000 Å. After depositing a 50 nm sputtered SiO_2 layer, RTA was performed for two minutes at temperatures ranging from 650 to 750 °C. The increased temperature and reduced thickness of the protection layer led to a larger blue-shift. Furthermore, we confirmed that 1000 Å PECVD SiO_2 effectively prevents QWI.

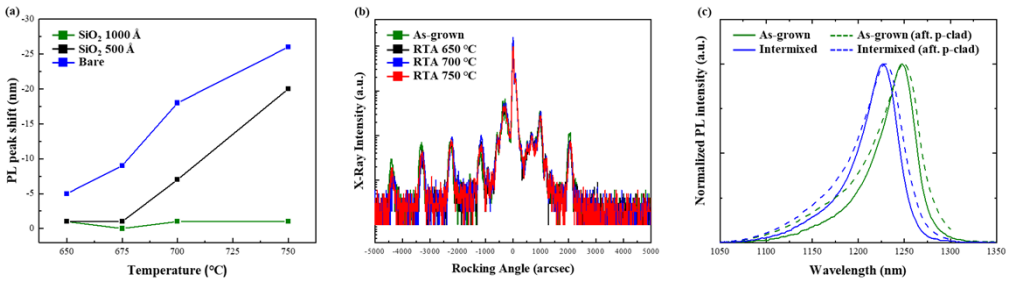

Fig. 1. (a) PL peak shift depending on the RTA temperature and SiO_2 layer thickness. (b) DXRD spectra of InAlGaAs MQWs before and after RTA. (c) PL spectra of as-grown and intermixed MQWs before and after p-clad growth.

Optics EXPRESS

Figure 1(b) presents the double crystal X-ray diffraction (DXRD) results for assessing the crystal quality in the as-grown and post-RTA conditions of bare samples. From the results, we observed identical satellite peaks of MQW after RTA, indicating there is no degradation in the crystal quality by the QWI process. Consequently, we applied the optimized conditions to the IA-EML fabrication and observed PL spectra with a wavelength difference of about 20 nm between the as-grown and intermixed MQWs (Fig. 1(c)). The PL peak wavelengths of the as-grown and intermixed MQWs are approximately 1247 and 1227 nm, respectively. Moreover, as seen in Fig. 1(c), there is no shift in the PL peaks even after the p-cladding layer growth (2 μm at 600 °C). This indicates the absence of residual defects affecting the additional wavelength shift after the QWI process. In conclusion, our optimized IFVD-based QWI process demonstrates the potential for effective integrated device fabrication without degradation that could affect the quality of the epitaxial layers and device reliability.

3. Device design and fabrication

Figure 2(a) presents a schematic illustration of an IA-EML device, which comprises a distributed feedback (DFB) LD, WG, and EAM. The MQW consists of seven compressively strained InAlGaAs wells and eight tensile strained InAlGaAs barriers, grown using metal-organic chemical vapor deposition (MOCVD). The DFB LD region features an asymmetric λ/4 phase-shifted (APS) grating on top of an InGaAsP etch stop layer, patterned using electron beam lithography. The phase-shifted region is located at two-thirds of the length from the output facet of the DFB LD. The device has high-reflection (HR) and anti-reflection (AR) coatings on the rear and front facets, respectively. The APS grating and facet coatings enhance the optical mode power inside the cavity. Unlike conventional symmetric grating structures, the APS grating structure provides sufficient grating grids in the output direction, preventing degradation of the single-mode lasing characteristics caused by strong reflection at the HR-coated rear facet. The top ohmic layer of the WG is etched, and the device includes separate p-type contact metal pads to ensure electrical isolation between the DFB LD and the EAM. Additionally, the bottom of the metal pads is filled with benzocyclobutene (BCB), and the EAM pad diameter is minimized to 80 μm to reduce the parasitic capacitance of the device for 25 Gb/s operation. The n-type contact metal of the entire device is shared through the backside of the n-InP substrate. Figure 2(b) shows a scanning electron microscope (SEM) image of the fabricated device, featuring DFB LD, EAM, and WG lengths of 300, 100, and 70 μm, respectively.

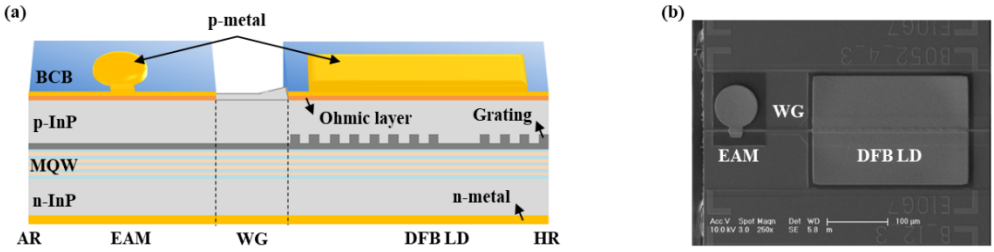

Fig. 2. (a) Schematic illustration of IA-EML device. (b) SEM image of the fabricated IA-EML.

We fabricated two types of IA-EML with different QWI configurations to evaluate their effects on the optical and modulation performance. The first type features QWI applied solely to the WG region (EML_W), while the second type has QWI applied to both the WG and EAM regions (EML_{WE}), as depicted in Fig. 3. The intermixed regions have a blue-shifted wavelength in comparison to the DFB LD region.

Optics EXPRESS

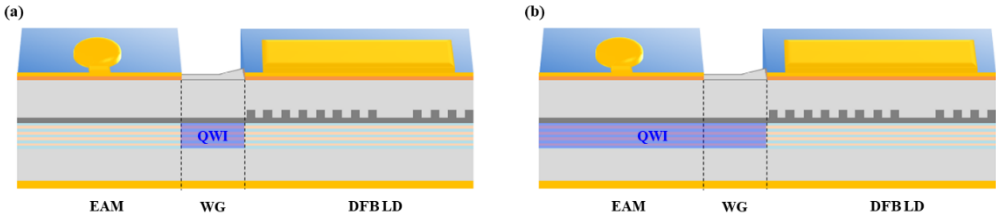

Fig. 3. Schematic representation of two types of IA-EML structures: (a) EML_W and (b) EML_{WE}. QWI applied (a) only WG and (b) both the WG and EAM regions in the IA-EML.

4. Results and discussion

4.1. Static characteristics

To verify the optical properties of the fabricated IA-EML chips, we preferentially analyzed the static characteristics of devices comprising as-grown and intermixed MQWs. First, to investigate the changes in the lasing properties after the fabrication, we manufactured a Fabry-Perot laser diode (FP LD) with a length of 300 μm on the same substrate as the IA-EML. Figure 4(a) shows the gain spectra of the FP LD comprising as-grown and intermixed MQWs, displaying a 20 nm wavelength difference, similar to the PL spectra in Fig. 1(c). Furthermore, we compared the temperature dependence of each FP LD and found that the as-grown and intermixed MQWs have characteristic temperatures (T_0) of 86.13 and 87.71 K, respectively (Fig. 4(b)). We confirmed the superior T_0 due to the strong confinement of electrons in the InAlGaAs MQW. Therefore, the chip has been optimized for efficient operation not only at 25 °C but also 45 °C.

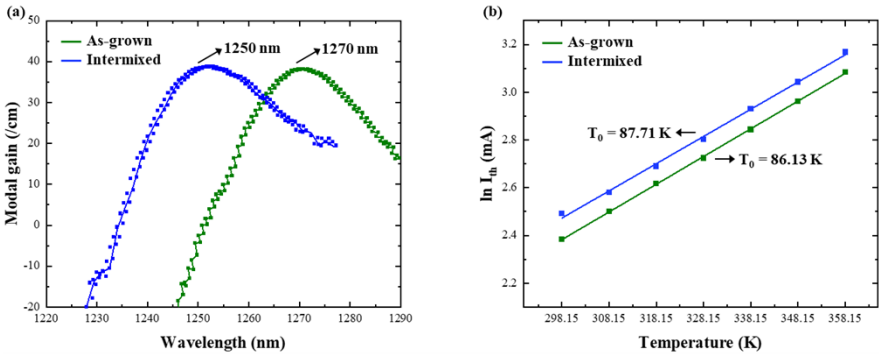

Fig. 4. (a) Gain spectra and (b) T_0 fitting curves of of 300 μm FP LD composed of as-grown and intermixed MQWs.

Figure 5 indicates the typical light versus current (L-I) curves and spectra of the two fabricated types of IA-EML. As the temperature was increased from 25 to 45 °C, the optical powers of the LD decreased from approximately 16 to 14 mW at a bias current of 100 mA, and the threshold current slightly increased from around 9 to 11 mA. The spectra in Fig. 5(b) show wavelengths of both types of IA-EML at the bias current of 60 mA. The single-mode lasing peaks of each device differ by less than 1 nm, and as the temperature rises by 20 °C, the lasing peaks shift 2 nm, moving from about 1291 to 1293 nm. Furthermore, the spectra maintain a stable single-mode emission with a side mode suppression ratio (SMSR) of over 40 dB at both temperatures.

We measured the static extinction ratio (ER) of the EAM to investigate its modulation properties, as shown in Fig. 6. The EML_W has a detuning of about 21 nm in gain wavelength reference of the EAM MQW at 25 °C. On the other hand, the EML_{WE} has a detuning value of approximately

Optics EXPRESS

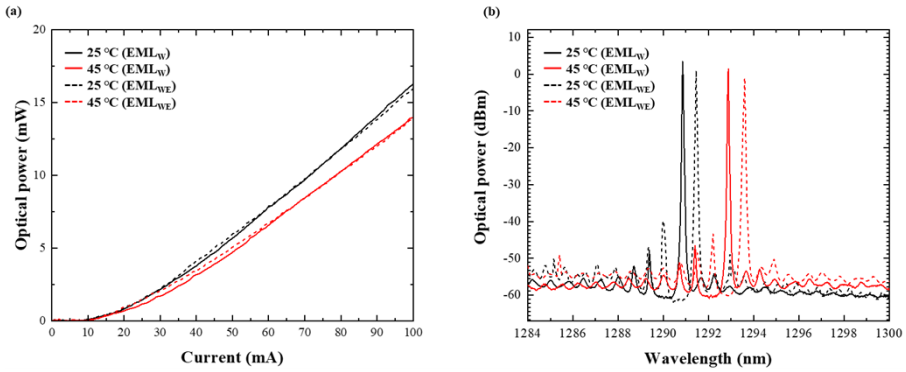

Fig. 5. (a) Typical L-I curves and (b) optical spectra of the EML_W and EML_{WE} at 25 and 45 °C.

41 nm at 25 °C. As the detuning increases, the reverse bias voltage for EAM absorption also increases due to the shift of the EAM absorption wavelength away from the DFB LD lasing wavelength, leading to a decrease in the static ER. We also observed that the operation voltage decreased as the temperature rose from 25 to 45 °C for both EMLs because of the red-shift of the absorption wavelength of the EAM. As a result, the EML_W shows a static ER of about -23 dB at both 25 and 45 °C within -4 V. Otherwise, the EML_{WE} has a static ER of -18 and -20 dB at 25 and 45 °C, respectively, at -4 V, exhibiting unsaturated forms. Therefore, when the EAM is intermixed, a higher reverse bias voltage is required, and the static ER decreases due to the reduced absorption efficiency. As a result of the influence of these limitations, we could not confirm the positive effects of the intermixed EAM in our QWI conditions. Consequently, we speculated that the absorption properties of EML_W would be more favorable for dynamic modulation compared to EML_{WE}.

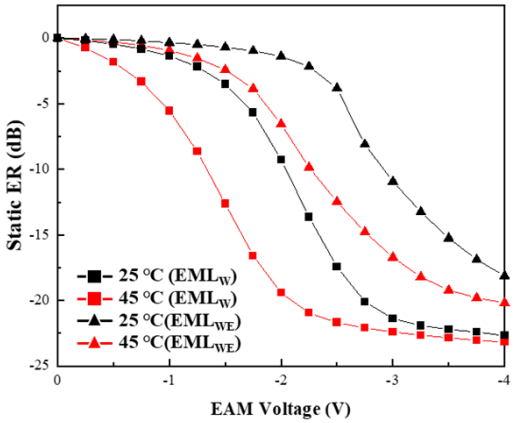

Fig. 6. Static ER characteristics of EML_W and EML_{WE} at 25 and 45 °C

4.2. Dynamic characteristics

To clarify the dynamic characteristics of the IA-EML, we performed 25 and 32 Gb/s NRZ and 26.56 Gbaud PAM4 (53 Gb/s) eye diagram measurements for back-to-back operations at temperatures of 25 and 45 °C. We analyzed the eye diagrams using a Keysight 86100D digital communication analyzer with an N1030A optical module and an Anritsu MU196020A pulsed

Optics EXPRESS

pattern generator. During the measurements, the IA-EML chip was mounted on an AlN submount and connected to a ground-signal-ground line, as well as a 50 Ω load matching resistor for RF signal injection.

Before examining the EML_W and EML_{WE}, we have confirmed the dynamic characteristics of the IA-EML without QWI, which have same device structure and detuning condition. Figure 7(a) presents the non-filtered eye diagrams of the 25 Gb/s NRZ signal at 25 and 45 °C. We observed significantly degraded eye diagrams, which hinder the analysis of clear dynamic performance of the device, due to the small detuning value of approximately 21 nm for the IA-EML operation. The 3 dB bandwidth also exhibits low values of 11.60 and 8.92 GHz at 25 and 45 °C, respectively (Fig. 7(b)). One of obvious reasons for these unfavorable results is the deterioration of dynamic characteristics due to the influence of the absorptive waveguide [21]. As a general solution, a substantial detuning is applied to address this issue. However, in our case, we implemented QWI process to enhance performance while maintaining the same detuning.

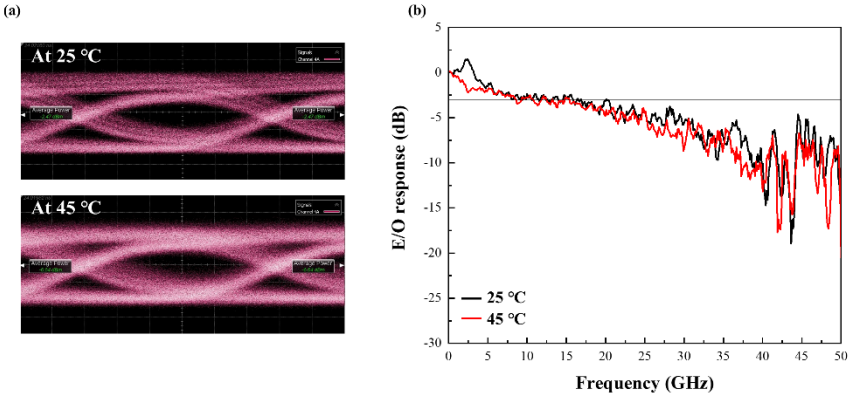

Fig. 7. (a) EYE diagrams of 25 Gb/s NRZ signal and (b) small-signal EO responses of IA-EML without QWI at 25 and 45 °C.

Figure 8 displays the non-filtered eye diagram for (a) EML_W and (b) EML_{WE}, obtained under 25 Gb/s modulation at 25 and 45 °C. The peak-to-peak voltage (V_{pp}) is 2.80 V and is amplified four times through a 12 dB linear amplifier. First of all, compared to the results in Fig. 7, both types of EML demonstrate clearer eye diagrams. This strongly suggests that the eliminating the absorptive WG allows for improved dynamic performance even at the small detuning value of about 21 nm. The EML_W has dynamic ERs of 8.59 and 8.45 dB at 25 and 45 °C, respectively. Meanwhile, the EML_{WE} shows dynamic ERs of 7.16 and 6.85 dB at 25 and 45 °C, respectively. As the temperature increases from 25 to 45 °C, the reverse bias voltage decreases by approximately 0.53 V. At this point, the dynamic ER of the EML_W is nearly maintained. Based on the results, the EML_{WE} necessitates an average applied reverse bias voltage that is about 0.95 V higher than that of the EML_W. This occurs because the MQW of the EAM is shifted by about -20 nm in wavelength, requiring more reverse bias voltage for absorption modulation at the lasing wavelength. Moreover, the dynamic ER decreases due to the large detuning of the gain peak and lasing wavelength of more than 40 nm, resulting in a decline in the absorption efficiency.

The eye diagrams in Fig. 9 show the non-filtered results under 32 Gb/s modulation at 25 and 45 °C. The applied reverse bias voltage is the same as the condition under 25 Gb/s modulation. For the EML_W, voltages of -2.18 and -1.60 V, and for the EML_{WE}, -3.07 and -2.60 V are applied at 25 and 45 °C, respectively. The 32 Gb/s modulation eye diagrams exhibit a similar trend to the previous results, with the dynamic ER of the EML_W exceeding 7.60 dB and being higher than that of the EML_{WE}. The results from the NRZ eye diagrams reveal that the EML_W demonstrates an improved dynamic ER under the optimal conditions at 25 and 45 °C, compared to EML_{WE}.

Optics EXPRESS

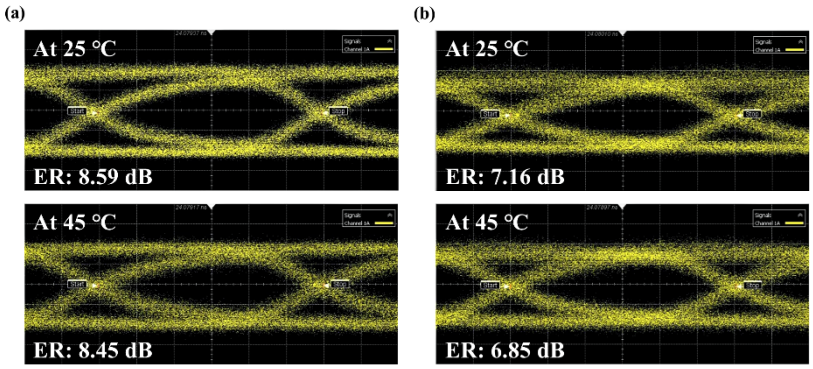

Fig. 8. EYE diagrams of 25 Gb/s NRZ signal at LD current of 60 mA and V_{pp} of 2.80 V (a) EYE diagrams of EML_W at EAM bias of -2.18 and -1.60 V at 25 and 45 °C, respectively. (b) EYE diagrams of EML_{WE} at EAM bias of -3.07 and -2.60 V at 25 and 45 °C, respectively.

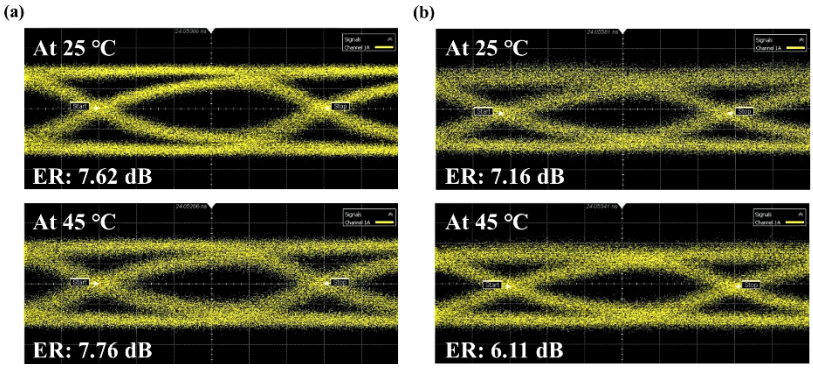

Fig. 9. EYE diagrams of 32 Gb/s NRZ signal at LD current of 60 mA and V_{pp} of 2.80 V (a) EYE diagrams of EML_W at EAM bias of -2.18 and -1.60 V at 25 and 45 °C, respectively. (b) EYE diagrams of EML_{WE} at EAM bias of -3.07 and -2.60 V at 25 and 45 °C, respectively.

In the NRZ eye diagrams in Figs. 8 and 9, we conjecture that the slightly insufficient rise time is due to the shallow ridge of the reverse mesa (RM) structure. The RM ridge structure is commonly used to reduce resistance caused by injected current. However, the more than twofold broader surface area leads to an increase in the capacitance of the IA-EML device, which results in slight degradation of its dynamic performance. There also exists the difficulty of sidewall passivation. These issues could be resolved by improving the ridge structure with a vertical type. Even if the resistance increases by the vertical structure, it could be optimized by adjusting the doping density and the thickness of the p-cladding layer. Moreover, we anticipate that the dynamic performance could be enhanced after the additional optimization of the epitaxial structure for IA-EML is also considered. Nevertheless, we have confirmed the clear NRZ eye diagram at 25 and 32 Gb/s and conducted EO response measurements to validate 3 dB bandwidth before verify further PAM4 eye diagrams.

Figure 10 illustrates the small-signal EO responses of EML_W and EML_{WE}. The 3 dB bandwidths for the EML_W at 25 and 45 °C are 19.79 and 17.54 GHz, respectively, whereas for the EML_{WE}, they are 18.92 and 16.99 GHz. Compared to Fig. 7, enhancements in the 3 dB bandwidth and high-temperature characteristics can be verified. When the temperature escalated from 25 to 45 °C, the bandwidth of the IA-EML without QWI decreased by about 23%, whereas the EML_W and EML_{WE} displayed a reduction of approximately 11%. This is attributed to the

Optics EXPRESS

amplified influence of the absorptive WG as the PL peak red-shifts with rising temperature. In the same trends with eye diagram results (Fig. 8 and 9), the EML_W displays slightly superior or comparable performance to the EML_{WE}, and both configurations demonstrate exceptional temperature characteristics. The bias voltage for the EML_W at 25 and 45 °C is 2.00 and 1.50 V, respectively, while for the EML_{WE}, it is 3.00 and 2.50 V at the same temperatures. Given that the wavelength of the waveguide region is identical for both the EML_W and EML_{WE}, it suggests that the impact of the elimination of absorptive WG is similar in both devices. As a result, we speculate that the EML_W is a more suitable configuration for high-speed modulation, meeting the enhanced dynamic ER and 3 dB bandwidth at a lower driving voltage.

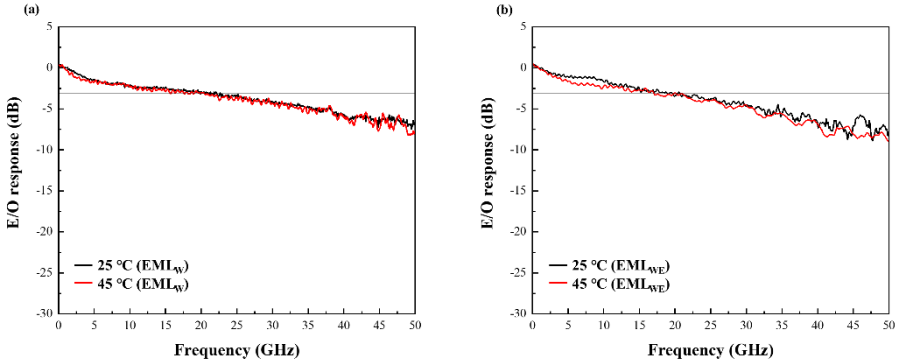

Fig. 10. Small-signal EO response of (a) EML_W and (b) EML_{WE} with an LD current of 60 mA at 25 and 45 °C.

Figure 11 presents the 26.56 Gbaud PAM4 eye diagram obtained using a fourth-order-Bessel-Thomson (13.3 GHz) filter and a 5-Tap T-spaced feed forward equalizer (FFE) based on IEEE 802.3cd [41]. The measurements were conducted at 25 and 45 °C for both EML_W and EML_{WE}. Clear eye openings were observed for all results at both temperatures. Furthermore, the EML_W exhibits a higher outer ER of 7.57 and 8.01 dB at 25 and 45 °C, respectively, at lower reverse bias voltages than the EML_{WE}. Both devices have clear PAM4 eye diagrams and a sufficient outer ER because of the high linearity of the absorption modulator characteristics and a static ER suitable for PAM4 as well as NRZ modulation. Comparing the TDECQ values of the two configurations,

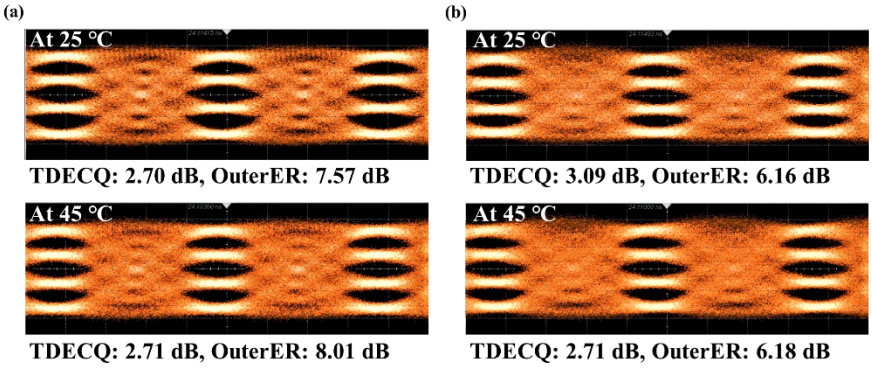

Fig. 11. EYE diagram of 26.56 Gbaud PAM4 signal at LD current of 60 mA and V_{pp} of 1.60 V (a) EYE diagrams of EML_W at EAM bias -2.37 and -1.75 V at 25 and 45 °C, respectively. (b) EYE diagrams of EML_{WE} at EAM bias -3.18 and -2.70 V at 25 and 45 °C, respectively.

Optics EXPRESS

we found that the EML_W had lower values at both 25 and 45 °C, measuring 2.70 and 2.71 dB, respectively, compared to the values of 3.09 and 2.71 dB for the EML_{WE}. These results suggest that the EML_W exhibits optimal dynamic characteristics by maintaining appropriate detuning. In conclusion, our results confirm that inhibition of WG absorption through QWI contributes to enhancing the modulation properties of the IA-EML.

5. Conclusion

In this study, we propose an IA-EML that includes a QWI region to eliminate absorptive WG without utilizing butt-joint regrowth. We carried out an optimized IFVD method prior to the p-clad growth to perform minimal QWI, avoiding damage to the active layers. The InAlGaAs MQW showed a blue-shift of 20 nm in PL and gain wavelength spectra after the QWI. Both as-grown and intermixed MQWs exhibited a T_0 exceeding 86 K, confirming the superior high-temperature performance of InAlGaAs materials. To compare the effects of intermixed regions on the IA-EML, we fabricated IA-EMLs not only without QWI but also with an intermixed WG, and with both an intermixed WG and EAM. For both types of intermixed IA-EML, 25 and 32 Gb/s NRZ and 26.56 Gbaud PAM4 eye diagrams revealed modulation characteristics devoid of WG absorption, even with small detuning of less than 25 nm between the gain and lasing wavelength. Notably, the EML_W exhibited a higher ER than the EML_{WE}, even at a lower driving voltage. Moreover, it demonstrated optimized NRZ and PAM4 eye diagrams not only at 25 °C but also 45 °C. Our study suggests that implementing the proper QWI in the IA-EML is a promising approach for eliminating the absorptive WG without any complicated regrowth process, as well as for the monolithic integration of various photonic devices.

Funding. Ministry of Science and ICT, South Korea (2021-0-00826).

Acknowledgments. This work was supported by Institute of Information & Communications Technology Planning & Evaluation (IITP) grant funded by the Korea government (MSIT; Ministry of Science and ICT) (NO. 2021-0-00826).

Disclosures. The authors declare no conflicts of interest.

Data availability. Data underlying the results presented in this paper are not publicly available at this time but may be obtained from the authors upon reasonable request.

References

1. X. Liu, "Enabling optical network technologies for 5 G and beyond," J. Lightwave Technol. **40**(2), 358–367 (2022).
2. J. Huang, C. Li, R. Lu, L. Li, and Z. Cao, "Beyond the 100 Gbaud directly modulated laser for short reach applications," J. Semicond. **42**(4), 041306 (2021).
3. O. K. Kwon, C. W. Lee, and K. S. Kim, "Electroabsorption modulator-integrated distributed Bragg reflector laser diode for C-band WDM-based networks," ETRI J. **45**(1), 163–170 (2023).
4. K. Zhong, X. Zhou, J. Hao, C. Yu, C. Lu, and A. P. T. Lau, "Digital signal processing for short-reach optical communications: A review of current technologies and future trends," J. Lightwave Technol. **36**(2), 377–400 (2018).
5. Y. Han, Q. Tian, S. Yang, J. Luan, R. Zhang, P. He, D. Liu, and M. Zhang, "Direct modulation bandwidth enhancement of uncooled DFB laser operating over a wide temperature range based on groove-in-trench waveguide structure," Opt. Express **30**(9), 15757–15765 (2022).
6. X. Dai, H. Debregeas, G. Da Rold, D. Carrara, K. Louarn, E. D. Valdeiglesias, and F. Lelarge, "Versatile externally modulated lasers technology for multiple telecommunication applications," IEEE J. Select. Topics Quantum Electron. **27**(3), 1–12 (2021).
7. T. L. Koch and E. Bowers, "Nature of wavelength chirping in directly modulated semiconductor lasers," Electron. Lett. **20**(25-26), 1038–1040 (1984).
8. K. Sato, S. Kuwahara, and Y. Miyamoto, "Chirp characteristics of 40-Gb/s directly modulated distributed-feedback laser diodes," J. Lightwave Technol. **23**(11), 3790–3797 (2005).
9. T. Ishikawa and J. E. Bowers, "Band lineup and in-plane effective mass of InGaAsP or InGaAlAs on InP strained-layer quantum well," IEEE J. Quantum Electron. **30**(2), 562–570 (1994).
10. W. Kobayashi, M. Arai, T. Yamanaka, N. Fujiwara, T. Fujisawa, T. Tadokoro, K. Tsuzuki, Y. Kondo, and F. Kano, "Design and fabrication of 10-/40-Gb/s, uncooled electroabsorption modulator integrated DFB laser with butt-joint structure," J. Lightwave Technol. **28**(1), 164–171 (2010).
11. T. Fujisawa, S. Kanazawa, W. Kobayashi, K. Takahata, A. Ohki, R. Iga, and H. Ishii, "50 Gbit/s uncooled operation (5–85° C) of 1.3 μm electroabsorption modulator integrated with DFB laser," Electron. Lett. **49**(3), 204–205 (2013).

Optics EXPRESS

12. B. K. Saravanan, T. Wenger, C. Hanke, P. Gerlach, M. Peschke, and R. Macaluso, "Wide temperature operation of 40-Gb/s 1550-nm electroabsorption modulated lasers," IEEE Photonics Technol. Lett. **18**(7), 862–864 (2006).
13. S. Kollakowski, C. Lemm, A. Strittmatter, E. H. Bottcher, and D. Bimberg, "Buried InAlGaAs-InP waveguides: etching, overgrowth, and characterization," IEEE Photonics Technol. Lett. **10**(1), 114–116 (1998).
14. K. Yashiki, T. Kato, H. Chida, K. Tsuruoka, R. Kobayashi, S. Sudo, K. Sato, and K. Kudo, "10-Gb/s 23-km penalty-free operation of 1310-nm uncooled EML with semi-insulating BH structure," IEEE Photonics Technol. Lett. **18**(1), 109–111 (2006).
15. Y. Zhang, F. Yang, G. Liu, G. Li, M. Xiang, Q. Lu, J. F. Donegan, and W. Guo, "Experimental Demonstration of an Easy-to-Fabricate 1.3-μm Directly Modulated DFB Laser With Improved Beam Profile," J. Lightwave Technol. **41**(10), 3094–3101 (2023).
16. A. Ramdane, A. Ougazzaden, F. Devaux, F. Delorme, M. Schneider, and J. Landreau, "Very simple approach for high performance DFB laser-electroabsorption modulator monolithic integration," Electron. Lett. **30**(23), 1980–1981 (1994).
17. C. Sun, B. Xiong, J. Wang, P. Cai, J. Xu, J. Huang, He Yuan, Q. Zhou, and Yi Luo, "Fabrication and packaging of 40-Gb/s AlGaInAs multiple-quantum-well electroabsorption modulated lasers based on identical epitaxial layer scheme," J. Lightwave Technol. **26**(11), 1464–1471 (2008).
18. Q. Deng, Lu Guo, S. Liang, S. Sun, X. Xie, H. Zhu, and W. Wang, "AlGaInAs EML having high extinction ratios fabricated by identical epitaxial layer technique," Opt. Commun. **413**, 54–57 (2018).
19. S. Yang, C. Sun, B. Xiong, J. Zhang, J. Wang, Yi Luo, Z. Hao, Y. Han, L. Wang, H. Li, T. Tanemura, and Y. Nakano, "Gain-coupled 4× 25 Gb/s EML array based on an identical epitaxial layer integration scheme," IEEE J. Sel. Topics Quantum Elecetron. **25**(6), 1–2 (2019).
20. M. Baier, N. Grote, M. Moehrle, A. Sigmund, F. M. Soares, M. Theurer, and U. Troppenz, "Integrated transmitter devices on InP exploiting electro-absorption modulation," PhotoniX **1**(1), 4–11 (2020).
21. H. Fukano, Y. Akage, Y. Kawaguchi, Y. Suzaki, K. Kishi, T. Yamanaka, Y. Kondo, and H. Yasaka, "Low chirp operation of 40 Gbit/s electroabsorption modulator integrated DFB laser module with low driving voltage," IEEE J. Select. Topics Quantum Electron. **13**(5), 1129–1134 (2007).
22. J. H. Marsh, "Quantum well intermixing revolutionizes high power laser diodes," Laser Technik J. **4**(5), 32–35 (2007).
23. Z. Ahmad, R. L. Chao, Y. J. Hung, J. Chen, C. C. Wei, and J. W. Shi, "High-Speed Electro-Absorption Modulated Laser at 1.3 μm Wavelength Based on Selective Area Growth Technique," in *Photonics Conference* (IEEE, 2019) pp. 1–2.
24. Q. Deng, H. Zhu, X. Xie, Lu Guo, S. Sun, S. Liang, and W. Wang, "Low chirp EMLs fabricated by combining SAG and double stack active layer techniques," IEEE Photonics J. **10**(2), 1–7 (2018).
25. T. Tsuchiya, J. Shimizu, M. Shirai, and M. Aoki, "InGaAlAs selective-area growth on an InP substrate by metalorganic vapor-phase epitaxy," J. Crystal Growth **276**(3-4), 439–445 (2005).
26. J. H. Marsh, "Quantum well intermixing," Semicond. Sci. Technol. **8**(6), 1136–1155 (1993).
27. Y. Alahmadi and P. LiKamWa, "Effects of selective area intermixing on InAlGaAs multiple quantum well laser diode," Semicond. Sci. Technol. **34**(2), 025010 (2019).
28. S. Arafin and L. A. Coldren, "Advanced InP photonic integrated circuits for communication and sensing," IEEE J. Select. Topics Quantum Electron. **24**(1), 1–12 (2018).
29. L. Hou, M. Haji, J. Akbar, J. H. Marsh, and A. C. Bryce, "AlGaInAs/InP monolithically integrated DFB laser array," IEEE J. Quantum Electron. **48**(2), 137–143 (2012).
30. X. Sun, S. Ye, W. Cheng, S. Liang, Y. Huang, B. Qiu, Z. Liu, J. Xiong, X. Liu, J. H. Marsh, and L. Hou, "Monolithically integrated AlGaInAs MQW polarization mode converter using a stepped height ridge waveguide," IEEE Photonics J. **14**(3), 1–6 (2022).
31. J. Decobert, G. Binet, A. D. B. Maia, P.-Y. Lagrée, and C. Kazmierski, "AlGaInAs MOVPE selective area growth for photonic integrated circuits," Adv. Opt. Techn. **4**(2), 167–177 (2015).
32. F. Lemaitre, C. Fortin, N. Lagay, G. Binet, D. Pustakhod, J. Decobert, H. Ambrosius, and K. Williams, "Foundry photonic process extension with bandgap tuning using selective area growth," IEEE J. Select. Topics Quantum Electron. **25**(5), 1–8 (2019).
33. Y. Cheng, Q. J. Wang, and J. Pan, "1.55 μm high speed low chirp electroabsorption modulated laser arrays based on SAG scheme," Opt. Express **22**(25), 31286–31292 (2014).
34. H. Zhao, S. Pinna, F. Sang, B. Song, S. T. Š. Brunelli, L. A. Coldren, and J. Klamkin, "High-power Indium phosphide photonic integrated circuits," IEEE J. Select. Topics Quantum Electron. **25**(6), 1–10 (2019).
35. C. Besancon, D. Néel, D. Make, J. M. Ramírez, G. Cerulo, N. Vaissiere, D. Bitauld, F. Pommereau, F. Fournel, C. Dupré, H. Mehdi, F. Bassani, and J. Decobert, "AlGaInAs multi-quantum well lasers on silicon-on-insulator photonic integrated circuits based on InP-seed-bonding and epitaxial regrowth," Appl. Sci. **12**(1), 263 (2021).
36. Y.-J. Chen, R.-Y. Chen, C.-C. Shiu, W.-K. Hsu, W.-C. Lin, Y.-H. Lin, T.-C. Chang, and Y.-J. Chiu, "Supercritical fluid-enhanced IFVD quantum well intermixing for the regrowth-free photonic integration of EAM and SOA," Opt. Mater. Express **8**(9), 2592–2599 (2018).
37. N. Sekine, K. Sumita, K. Toprasertpong, S. Takagi, and M. Takanaka, "Monolithic integration of electro-absorption modulators and photodetectors on III-V CMOS photonics platform by quantum well intermixing," Opt. Express **30**(13), 23318–23329 (2022).

Optics EXPRESS

38. J. W. Raring, L. A. Johansson, E. J. Skogen, M. N. Sysak, H. N. Poulsen, S. P. DenBaars, and L. A. Coldren, "40-Gb/s widely tunable low-drive-voltage electroabsorption-modulated transmitters," J. Lightwave Technol. **25**(1), 239–248 (2007).
39. X. Sun, W. Cheng, Y. Sun, S. Ye, A. Al-Moathin, Y. Huang, R. Zhang, S. Liang, B. Qiu, J. Xiong, X. Liu, J. H. Marsh, and L. Hou, "Simulation of an AlGaInAs/InP Electro-Absorption Modulator Monolithically Integrated with Sidewall Grating Distributed Feedback Laser by Quantum Well Intermixing," Photonics **9**(8), 564 (2022).
40. L. A. Coldren, S. C. Nicholes, L. Johansson, S. Ristic, R. S. Guzzon, E. J. Norberg, and U. Krishnamachari, "High Performance InP-Based Photonic ICs—A Tutorial," J. Lightwave Technol. **29**(4), 554–570 (2011).
41. "IEEE 802.3cd 50 Gb/s, 100 Gb/s, and 200 Gb/s ethernet task force," (2018), http://www.ieee802.org/3/cd/.